Available online at www.sciencedirect.com
ScienceDirect
Trans. Nonferrous Met. Soc. China 24(2014) 1512−1520
Transactions of Nonferrous Metals Society of China
www.tnmsc.cn

Effects of geometric parameters and axial magnetic field on buoyant−thermocapillary convection during detached solidification

Zhen LI, Lan PENG, You-rong LI

Key Laboratory of Low-grade Energy Utilization Technologies and Systems of Ministry of Education, Chongqing University, Chongqing 400044, China

Received 30 January 2013; accepted 26 May 2013

Abstract: In order to understand the effect of geometric parameters and axial magnetic field on buoyant−thermocapillary convection during detached solidification, a series of three-dimensional numerical simulations were conducted by the finite-difference method. The results indicate that the stable flow is observed when the Marangoni number (*Ma*) is small; however, when the value of *Ma* increases and exceeds a threshold value, the stable steady flow transits to be unstable flow. As the height of the melt increases, the flow is enhanced at first and then gets weakened. As the width of gap decreases gradually, the strength of flow is enhanced. The approach of using axial magnetic field is an effective way to suppress the buoyant−thermocapillary convection. As the magnetic field strength increases, the inhibition is enhanced. The critical Marangoni number increases slightly with a greater melt height, a narrower width of gap, and a more strength of magnetic field.

Key words: crystal growth; detached solidification; buoyant−thermocapillary convection; axial magnetic field

1 Introduction

Detached solidification technique is a crystal growth method combining the advantages of both the Czochralski and vertical Bridgman methods. It is benefit for the growth of II−VI compounds semiconductor materials such as CdZnTe. This method was firstly discovered in the experiments of crystal growth, by Bridgman method under microgravity condition in 1974 [1,2]. SYLLA and DUFFAR [3] conducted a series of detached solidification experiments using GaSb and InSb in silicon crucible, and the results confirmed that the crystal quality obtained by detached solidification was greatly improved. To obtain CdZnTe crystal, GAMAL et al [4] adopted traditional Bridgman method and detached solidification method, respectively, and found that the detached solidification method could greatly reduce the dislocation densities of the crystal, thus improving the quality of the crystal.

However, the coupled buoyancy and thermocapillary forces will drive the melt flow during detached solidification, and this flow has a direct impact on the quality of the growing single crystal, such as the undesired creation of striations. PENG et al [5,6] studied the thermocapillary flow in detached solidification of CdZnTe under microgravity and gravity by a series of two-dimensional numerical simulation. ZHANG et al [7] and STELIAN et al [8] studied the effect of temperature gradient on the melt flow during detached solidification under microgravity. In recent years, many studies about detached solidification method have been reported. However, study on buoyant−thermocapillary convection during detached solidification is less.

In recent years, it has been demonstrated that the magnetic field plays an important role in the fluid flow or heat and mass transfer in the electrically conductive fluids，which has already gained some achievements [9−12]. GELFGAT et al [13] studied the influence of axial magnetic field on the three-dimensional unstable natural convection flow. The results showed that when the magnitude of magnetic field exceeded a certain value, the unstable flow would switch to a steady flow. JABER et al [14] conducted a three-dimensional numerical simulation of the melt flow during GeSi crystal growth under the axial and rotating magnetic field and the results exhibited that the magnetic field can effectively suppress the melt flow. SANKAR et al [15] studied the effect of

Foundation item: Project (51076173) supported by the National Natural Science Foundation of China
Corresponding author: Lan PENG; Tel: +86-23-65112813; Fax: +86-23-65102473; E-mail: penglan@cqu.edu.cn
DOI: 10.1016/S1003-6326(14)63220-9

magnetic field on the buoyancy and thermocapillary driven convection in annular enclosure, and the results indicated that magnetic fields could effectively suppress the flow. PENG et al [16,17] investigated the effect of magnetic field on the melt flow during detached solidification under microgravity and the results showed that the axial magnetic field and the cusp magnetic field could suppress the melt flow and improve the crystal quality. Although a lot of researches have been done to suppress the fluid flow in an electrically conductive fluid using magnetic field, there are few publications reported about influence of the magnetic field on the flow during detached solidification process.

Therefore, the main purpose of the present study is to investigate the effect of geometric parameters and axial magnetic field on the buoyant−thermocapillary convection of CdZnTe melt in detached solidification. Finite-difference method is adopted to simulate the three-dimensional thermocapillary flow of CdZnTe melt under gravity.

2 Physical and mathematical models

The simplified model of detached Bridgman crystal growth, as shown in Fig. 1, is adopted in the present study. There, h is the height of melt, r_o is the radius of crucible, r_i is the radius of crystal and b is the width of gap. The crucible wall and the solidification front are maintained at a constant temperature T_h and T_m ($T_h>T_m$), respectively. The axial magnetic field is from the bottom up through the melt.

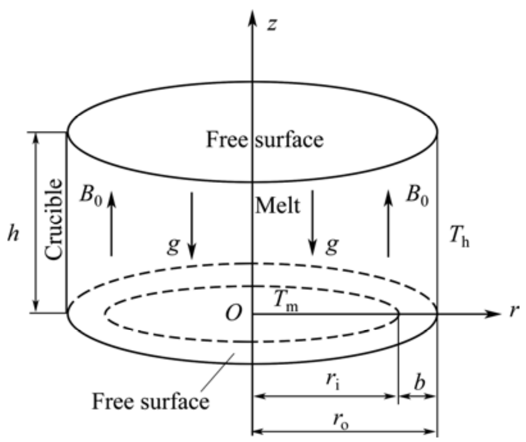

Fig. 1 Physical model of simulation system

For the convenience of computing, the assumptions are as follows: 1) The melt is incompressible Newtonian fluid; 2) Constant properties except both the surface tension and density are linear functions of temperature; 3) The free surfaces (including both the top and gap faces) are non-deformable and adiabatic; 4) Thermocapillary force acts on the free surface and no-slip boundary conditions are applied to solid−liquid interfaces; 5) The flow is assumed to be laminar; 6) All boundaries are considered electrically insulating.

With the above assumptions, the fluid flow in CdZnTe melt could be described by the dimensionless three-dimensional governing equations:

$$\nabla\cdot\boldsymbol{V}=0 \tag{1}$$

$$\frac{\partial\boldsymbol{V}}{\partial\tau}+\boldsymbol{V}\cdot\nabla\boldsymbol{V}=-\nabla P+\nabla^2\boldsymbol{V}-Ha^2\left(-\frac{\partial\phi}{\partial R}e_\theta+\frac{1}{R}\frac{\partial\phi}{\partial\theta}e_R+V_Re_R+V_\theta e_\theta\right)+Gr\Theta e_Z \tag{2}$$

$$\frac{\partial\Theta}{\partial\tau}+\boldsymbol{V}\cdot\nabla\Theta=\frac{1}{Pr}\nabla^2\Theta \tag{3}$$

The boundary conditions are as follows:

On the top surface ($Z=H$, $0<R<1$, $0\le\theta<2\pi$):

$$V_Z=0,\ \frac{\partial V_R}{\partial Z}=-\frac{Ma}{B\cdot Pr}\frac{\partial\Theta}{\partial R},\ \frac{\partial V_\theta}{\partial Z}=-\frac{Ma}{B\cdot Pr}\frac{\partial\Theta}{R\partial\theta},\ \frac{\partial\Theta}{\partial Z}=0,\ \frac{\partial\phi}{\partial Z}=0 \tag{4}$$

At the solidification interface ($Z=0$, $0<R\le R_i$, $0\le\theta<2\pi$):

$$V_R=V_\theta=V_Z=0,\ \Theta=0,\ \frac{\partial\phi}{\partial Z}=0 \tag{5}$$

At the gap ($Z=0$, $R_i<R<1$, $0\le\theta<2\pi$):

$$V_Z=0,\ \frac{\partial V_R}{\partial Z}=\frac{Ma}{B\cdot Pr}\frac{\partial\Theta}{\partial R},\ \frac{\partial V_\theta}{\partial Z}=\frac{Ma}{B\cdot Pr}\frac{\partial\Theta}{R\partial\theta},\ \frac{\partial\Theta}{\partial Z}=0,\ \frac{\partial\phi}{\partial Z}=0 \tag{6}$$

At the crucible wall ($R=1$, $0<Z<H$, $0\le\theta<2\pi$):

$$V_R=V_\theta=V_Z=0,\ \Theta=1,\ \frac{\partial\phi}{\partial R}=0 \tag{7}$$

The initial conditions ($\tau=0$) are:

$$V_R=V_\theta=V_Z=0,\ \Theta=0,\ \phi=0 \tag{8}$$

where (R, Z, θ) is the non-dimensional cylindrical coordinates; $\boldsymbol{V}$, P, Θ and τ are the non-dimensional velocity vector, pressure, temperature and time, respectively; H and B are the height of melt and the width of gap in non-dimensional form, respectively. All of them could be non-dimensionlized by the following formulas: $H=h/r_o$, $B=(r_o-r_i)/r_o$, $\boldsymbol{V}=\boldsymbol{v}r_o/\upsilon$, $P=pr_o^2/(\rho\upsilon^2)$, $\Theta=(T-T_m)/(T_h-T_m)$, $\tau=t\upsilon/r_o^2$, where t is the time.

The non-dimensional parameters, $Pr=\upsilon/\alpha$, $Ma=\gamma_T(T_h-T_m)(r_o-r_i)/\mu\alpha$, $Gr=g\beta(T_h-T_m)r_o^3/\upsilon^2$, $Ha=B_0r_o\sqrt{\sigma/(\rho\nu)}$, are the Prandtl number, Marangoni number, Grashof number and Hartmann number, respectively. $\gamma_T=-\partial\gamma/\partial T$ is the temperature coefficient of the surface tension and σ is the electric conductivity of melt. ϕ is the electric potential, which can be calculated using the following formulas: $\boldsymbol{J}=\sigma(-\nabla\phi+\boldsymbol{V}\times\boldsymbol{B})$, $\nabla\cdot\boldsymbol{J}=0$, $\Delta\phi=B_0 e_z\cdot\nabla\times\boldsymbol{V}$, $\boldsymbol{B}$=(0, 0, B_0). The non-dimensional stream function ψ is defined as: $V_R=-\partial\psi/(R\partial Z)$, $V_Z=\partial\psi/(R\partial R)$.

In this numerical simulation, the physical properties of CdZnTe melt are shown in Table 1. The values of non-dimensional geometric parameters for the physical model are as follows: 1) the width of gap, B=0.1, 0.075, 0.05 and 0.025; 2) the height of the melt, H=1.0, 2.0 and 3.0.

Table 1 Physical properties of CdZnTe melt

Parameter	Symbol	Value
Thermal expansion coefficient/K^{-1}	β	5.0×10^{-4}
Temperature coefficient	γ_T	0.14×10^{-3}
Density/(kg·m^{-3})	ρ	5.68×10^{3}
Thermal conductivity/(W·m^{-1}·K^{-1})	k	1.09
Melting temperature/K	T_m	1364
Specific heat capacity/(kJ·kg^{-1}·K^{-1})	c_p	0.187
Kinematic viscosity/(m^2·s^{-1})	ν	4.16×10^{-7}
Prandtl number	Pr	0.4

The dimensionless governing equations are discretized by the finite-difference method. The central difference approximation is adopted to the diffusion terms, while the QUICK scheme is used for the convective terms in these governing equations. The non-uniform grid used in the present work is $60^r\times50^z\times55^\theta$. To validate the grid convergence of numerical simulation, the maximum values of stream function (ψ_{max}) are evaluated with different grid systems when H=1, B=0.1, Ma=1×10^3 and Ha=0. The detailed results of grid convergence test are presented in Table 2. Obviously, the variation of these maximum values of the stream function with different numbers of grids is smaller than 5%, thus, the grid system used in this work is enough to satisfy the accuracy of the simulation results.

Table 2 Validation of grid convergence

Grid number	ψ_{max}	Relative error/%
$40^r\times40^z\times43^\theta$	9.77	−
$60^r\times50^z\times55^\theta$	11.66	16.21
$80^r\times60^z\times63^\theta$	12.01	2.90

3 Results and discussion

Once the temperature gradient is presented, the surface tension gradient is formed on the free surface, resulting in the thermocapillary convection in the flow field. Meanwhile, the buoyancy convection is generated due to the difference of melt density under gravity condition.

3.1 Stable buoyant−thermocapillary convection and flow instability

In order to study the flow patterns and temperature distributions of the buoyant−thermocapillary convection in the melt, the distribution profiles of streamlines and isotherms on the (R−Z)-plane with different Marangoni number are shown in Fig. 2, in the case of H=2, B=0.1 and Ha=0. It can be seen that two roll cells with opposite flow directions are formed in the melt due to the surface tension gradients on the free surfaces and buoyancy force; the upper roll cell rotates in the counterclockwise direction, while the other is in the clockwise direction. When Ma=1×10^2, the thermocapillary and buoyancy forces are very small and the buoyant-thermocapillary convection in the melt is very weak. The maximum value of the stream function is 3.02, and the intensity of the upper counterclockwise cell is stronger than that of the lower one. The distribution of the isotherms resembles the heat conduction profile, as shown in Fig. 2(a). With the increase of Marangoni number, the lower cell gradually expands to the center region of the melt. Due to the enhanced thermocapillary force, the melt flow is strengthened, and the amplitude of the enhanced strength of the lower cell is greater than that of the upper one. When the Marangoni number is increased to 1×10^3, the maximum value of the stream function reaches 12.04,

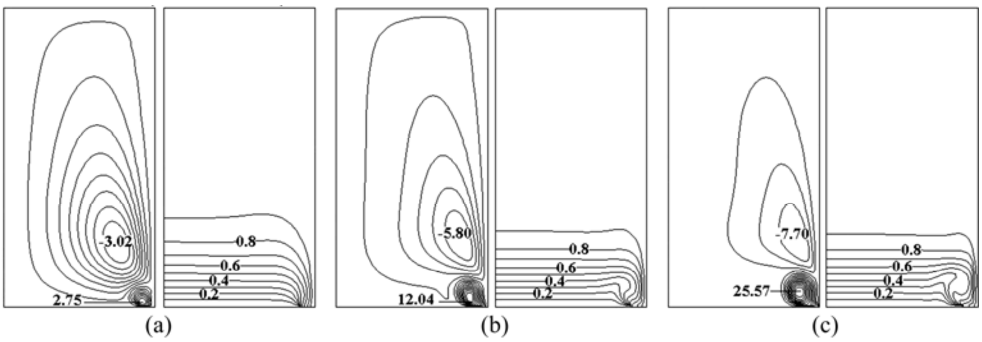

Fig. 2 Distribution of streamline (left) and isotherms (right) on (R−Z)-plane at H=2, B=0.1 and Ha=0, $\delta\psi=\psi_{max}/15$, $\delta\Theta$=0.1: (a) Ma=1×10^2; (b) Ma=1×10^3; (c) Ma=3×10^3

and the flow intensity of lower cell exceeds the upper cell. At the same time, with the increase of Marangoni number, the temperature gradient in the melt is increased, and the isotherms are distorted, as shown in Fig. 2(b). When the Marangoni number increases to 3×10^3, the flow is strengthened further, and the maximum value of the stream function reaches 25.57, as shown in Fig. 2(c). Due to the enhanced strength of the lower cell, the isotherms near the crucible's sidewall distorted seriously. Instead of conduction mode, the convection is dominant in the flow field.

Figure 3 shows the velocity distribution on the lower free surface for H=1, B=0.075 and Ha=0. It is obvious that the velocity on lower free surface decreases gradually in radial direction, and increases with the increase of Marangoni number. Figure 4 shows the distribution of the non-dimensional velocity when H=1, B=0.075 and Ha=0 at R=0.5. It can be seen that the velocity perturbation in the melt is growing, with the increase of the Marangoni number.

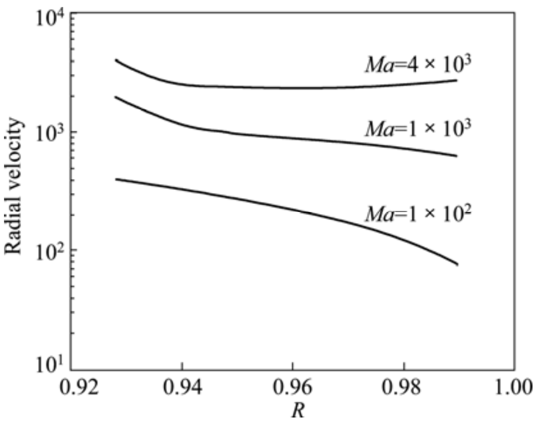

Fig. 3 Distribution of non-dimensional velocity on low free surface at H=1, B=0.075 and Ha=0

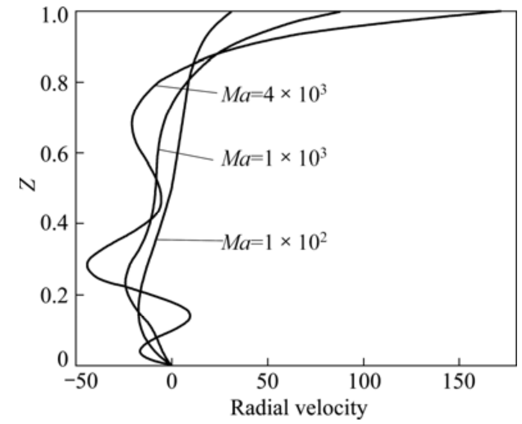

Fig. 4 Distribution of non-dimensional velocity for H=1, B=0.075 and Ha=0 at R=0.5

When the Marangoni number increases further and exceeds a critical value, the steady flow gradually transits to an oscillating flow due to the combined action of buoyancy and thermocapillary forces. In order to understand development of the flow characteristics with the increase of Marangoni number, distributions of isotherms on the cross section of Z=0.15 at H=2, B=0.1 and Ha=0 are shown in Fig. 5. As can be seen, isotherms are in relatively sparse concentric distribution (Fig. 5(a)) at $Ma=1\times10^3$. In this case, the melt flow is relatively weak and the heat transfer is mostly achieved by conduction. When $Ma=3\times10^3$, the isotherms near the crucible wall become relatively dense, but still show a concentric distribution. This indicates that the melt flow remains steady, except for the enhanced heat transfer between the melt and the crucible wall, which is caused by the strengthened convection heat transfer. But when $Ma=7.5\times10^3$, the non-axisymmetric isotherms distribution is observed on this cross section, which indicates that the stable flow transits to be unsteady flow, thereby affects the temperature distribution inside the melt, as shown in Fig. 5(c).

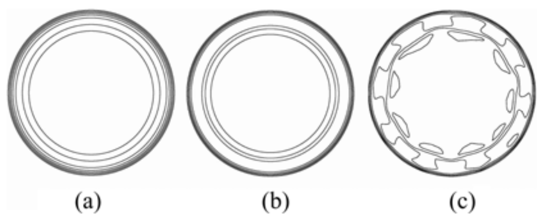

Fig. 5 Distributions of isotherms at H=2, B=0.1 and Z=0.15: (a) $Ma=1\times10^3$; (b) $Ma=3\times10^3$; (c) $Ma=7.5\times10^3$

To determine the critical Marangoni number (Ma_{cr}) when the flow transits from steady state to unsteady state, a certain number of monitoring points in the melt were selected, if the temperature and velocity of all the monitoring points stay constant, then the flow is steady; otherwise, it is unsteady. Therefore, in order to obtain high quality crystals, the Marangoni number of the flow should be controlled within the critical value. Figure 6 shows the radial velocity variation with time of a monitoring point (R=0.95, Z=0, θ=0) for H=1, B=0.1 and Ha=0 at $Ma=8\times10^3$, it can be seen that the velocity is

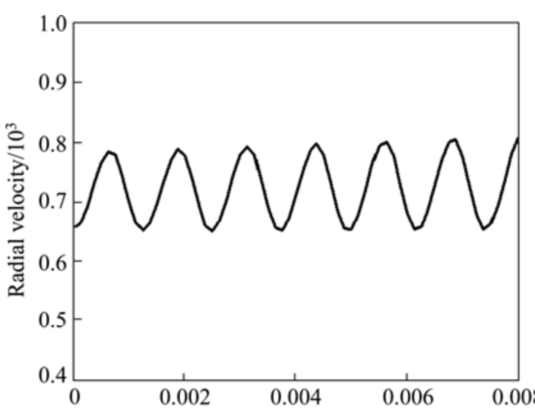

Fig. 6 Segment of non-dimensional velocity at R=0.95, Z=0 and θ=0

periodically oscillating, hence the flow is unsteady. By the variations of velocity and temperature with time of monitoring points, dichotomy is used to narrow the range of the critical Marangoni number. Then, the linear extrapolation method [18] can be used to accurately determine the critical Marangoni number of the buoyant−thermocapillary convection in the melt. For H=2, B=0.1 and Ha=0, the critical Marangoni number of the buoyant−thermocapillary convection in the melt is 4.07×10^3.

3.2 Effects of geometric parameters on buoyant−thermocapillary convection in melt

During detached solidification, the geometric parameters affecting buoyant−thermocapillary convection in the melt are mainly the height of the melt and the width of the gap. In order to understand the effect of melt height on buoyant−thermocapillary convection in the melt, the stream function and isotherms distribution on the (R−Z)-plane of the melt flow at B=0.1, Ma=1×10^3 and Ha=0 are shown in Fig. 7. It can be seen that, with the height of the melt increasing, the center of the upper roll cell will gradually move to the right and bottom. The intensity of the flow tends to increase first and then decrease, but the change is slight. Meanwhile, the isotherms distribution does not change obviously, indicating that the height of melt has limited influence on the buoyant−thermocapillary convection.

In order to investigate the influence of the width of gap on buoyant−thermocapillary convection in the melt, for H=1, Ma=1×10^3 and Ha=0, the stream function and isotherms distributions on the (R−Z)-plane at various width of gap are shown in Fig. 8. When B=0.1, the flow strength of the upper cell in the melt is weak. As the

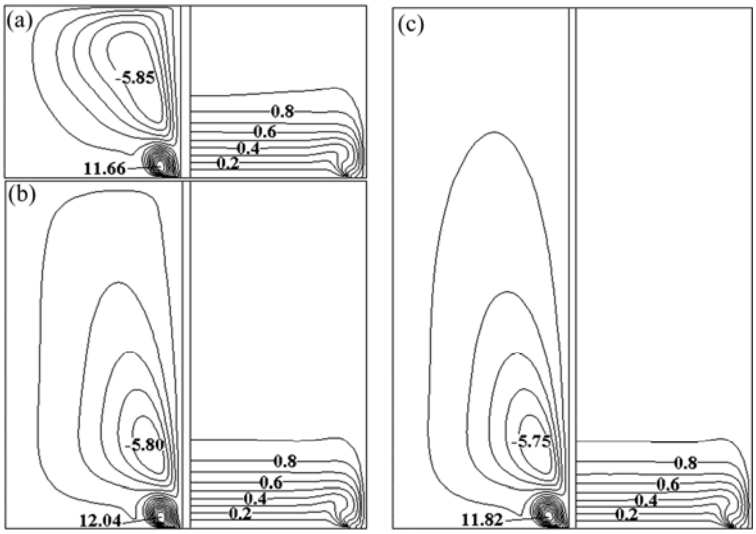

Fig. 7 Distributions of streamline (left) and isotherms (right) on (R−Z)-plane at B=0.1 and Ma=1×10^3, $\delta\psi=\psi_{max}/15$, $\delta\Theta$=0.1: (a) H=1; (b) H=2; (c) H=3

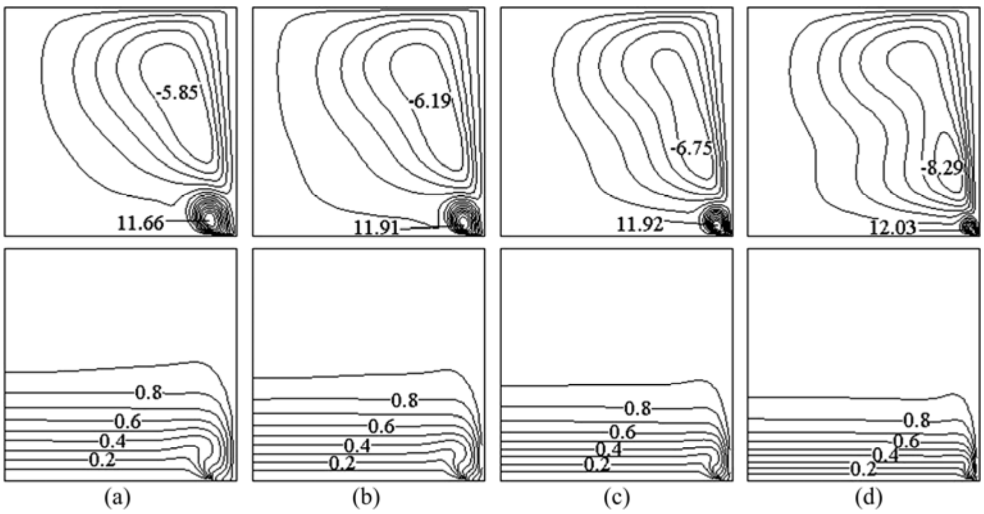

Fig. 8 Distributions of streamline (upside) and isotherms (downside) on (R−Z)-plane at H=1, Ma=1×10^3 and Ha=0, $\delta\psi=\psi_{max}/15$, $\delta\Theta$=0.1: (a) B=0.1; (b) B=0.075; (c) B=0.05; (d) B=0.025

width of gap decreases, the intensity of flow gradually strengthens, and the flow center of roll cells move to the right and bottom. This is because the decrease of the gap's width results in the increase of the temperature gradient on the free surface, thus, the flow driven by the thermocapillary force is stronger.

For H=2, Ma=1×10^2 and Ha=0, the radial velocity distributions on the lower free surface at different widths of gap are shown in Fig. 9. It is seen that the radial velocity on the upper free surface is reduced gradually along the radial direction, and with the width of gap decreasing, the velocity of the melt on the free surface increases. Figure 10 shows the variations of the radial velocity along the Z direction at different widths of gap when H=1, Ma=10^3 and Ha=0. It can be seen that, with the decrease in the width of gap, the internal disturbance of the melt is enhanced. Therefore, to improve the crystal quality during the detached solidification process, only from controlling of the flow in the melt, the lager value of the width of gap should be considered.

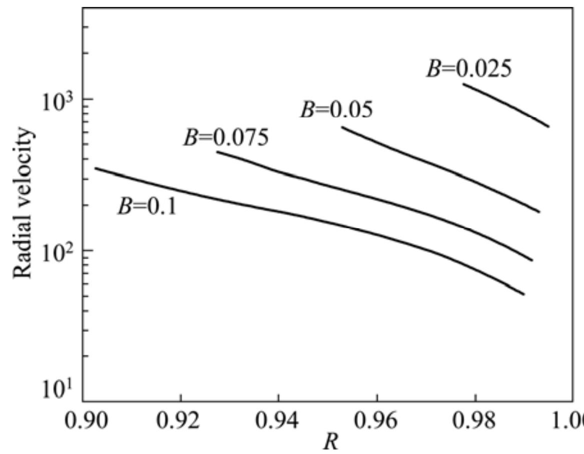

Fig. 9 Distribution of non-dimensional velocity on lower free surface at H=2, Ma=1×10^2 and Ha=0

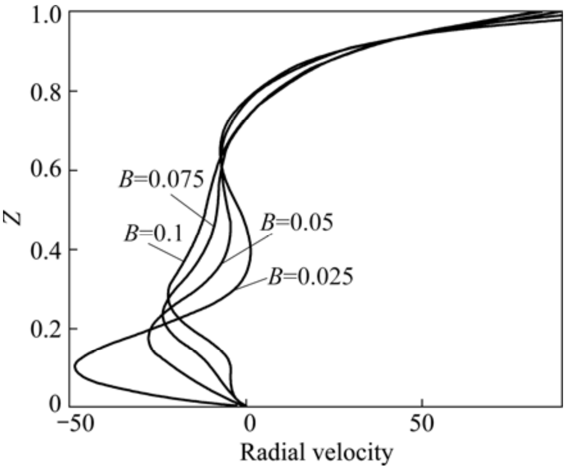

Fig. 10 Distribution of non-dimensional velocity for H=1, Ma=1×10^3 and Ha=0 at R=0.5

Furthermore, the geometric parameters also can affect the critical Marangoni number, as shown in Table 3. The critical Marangoni number increases slightly with a greater melt height, and increases with a narrower width of gap.

Table 3 Critical Marangoni number

H	B	$Ma_{cr}/10^3$			
		Ha=0	Ha=25	Ha=50	Ha=75
	0.1	3.86	6.41	16.2	65.5
1	0.075	4.38	7.96	24.5	71.0
	0.05	4.91	11.7	31.2	75.8
	0.1	4.17	6.47	17.3	66.3
2	0.075	4.44	8.05	25.8	73.4
	0.05	5.03	12.6	33.7	76.2

3.3 Effects of axial magnetic field on buoyant−thermocapillary convection

A number of studies have shown that the magnetic field can suppress the electrically conducting melt flow. In order to suppress the melt flow in detached solidification CdZnTe growth, and to improve the quality of the crystal, an axial magnetic field is imposed to inhibit the melt flow.

For H=2, B=0.1 and Ma=10^3, the distribution profiles of streamline and temperature on the (R−Z)-plane of melt with different Hartmann numbers are shown in Fig. 11. It also can be seen that two toroidal roll cells with opposite flow directions are formed in the melt due to the surface tension gradients on the free surfaces and buoyancy force. When Ha=0, the maximum value of stream function of the anticlockwise roll cell (the upper one) is −5.80, another roll cell is 12.04, as shown in Fig. 11(a). The intensity of roll cells weakens gradually as Hartmann number increases from 0 to 75 with 25 increment interval, and the maximum value of stream function decreases to −3.29 (anticlockwise) and 8.45 (clockwise), as shown in Figs. 11(b)−11(d). On the other hand, the temperature gradient near the solidification interface decreases with the increase of Hartmann number, as shown in Fig. 11 (downside). Based on the relationships between the streamline, temperature gradient and the value of Hartmann number, it could be clearly seen that the stability of the fluid flow in the melt could be improved by increasing the value of Hartmann number. For R=0.5, H=1, B=0.075, Ma=1×10^3, the distribution profiles of velocity with different Hartmann numbers are shown in Fig. 12. As can be seen that, with the imposed axial magnetic field, the internal disturbance in the melt is dramatically weakened. The higher Hartmann number results in the weaker disturbance.

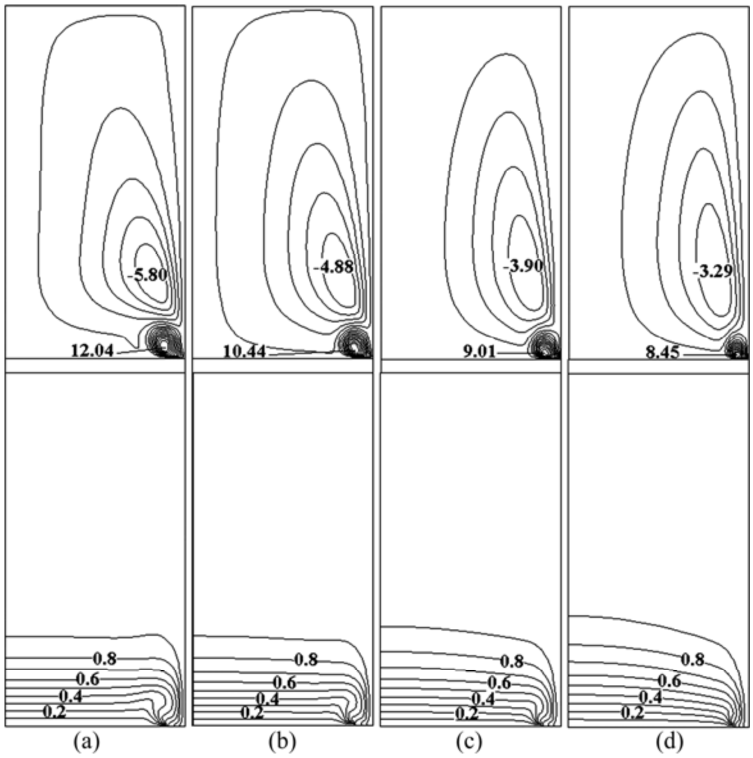

Fig. 11 Distributions of streamline (upside) and isotherms (downside) on (R−Z)-plane at H=2, B=0.1, and Ma=1×10^3, $\delta\psi=\psi_{max}/15$, $\delta\Theta$=0.1: (a) Ha=0; (b) Ha=25; (c) Ha=50; (d) Ha=75

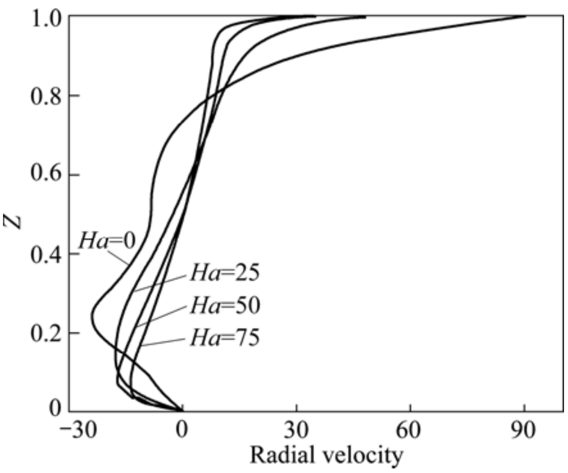

Fig. 12 Distribution of non-dimensional velocity for H=1, B=0.075 and Ma=1×10^3 at R=0.5

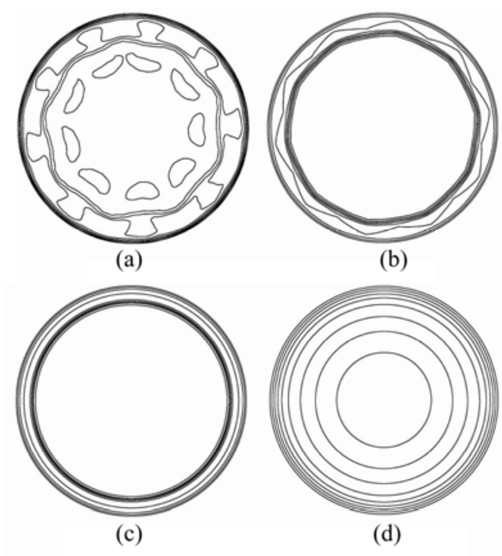

Fig. 13 Distributions of isotherms at H=1, Ma=1×10^4 and Z=0.2: (a) Ha=0; (b) Ha=25; (c) Ha=50; (d) Ha=75

In order to investigate the influence of magnetic field on the melt during detached solidification, a cross section of Z=0.2 is chosen, and the distributions of isotherms on this cross section at H=1, B=0.1 and Ma=1×10^4 with different values of Hartmann number are shown in Fig. 13. Obviously, when there is no magnetic field, the unstable flow is obtained and the non-axisymmetric isotherms distribution is observed and the shape of isotherms is like a tortoise with multiple feet, as shown in Fig. 13(a). However, once the magnetic field (Ha=25) is applied, the patterns of isotherms change and axisymmetric corrugated lines are observed, as shown in Fig. 13(b). As the intensity of magnetic field increases (i.e., Ha>50), the homocentric circularity distribution of isotherms appears, as shown in Figs. 13(c) and 13(d). This phenomenon indicates that the flow is unstable when there is no magnetic field; however, a stable flow could be obtained once the magnetic field is applied. The reason for this phenomenon is that the flow of electrically conductive fluid induces electric current in the present of magnetic field, and the Lorentz force will be generated due to this current in the melt. Since the direction of Lorentz force acting on the melt is opposite to that of thermocapillary force and buoyancy force, the buoyant−thermocapillary convection in the melt is suppressed. Therefore, a conclusion could be made that the magnetic field plays a positive role in the crystal growth.

On the other hand, the axial magnetic field not only can suppress the internal flow of melt effectively, but also has a major effect on the critical Marangoni number. The critical Marangoni numbers under different magnetic field strengths is shown in Table 3. The table reveals that with magnetic field strength increasing, the critical Marangoni number is increased by an order of magnitude at least.

4 Conclusions

1) Two toroidal roll cells with the opposite flow directions are formed in the melt. When the Marangoni number is small, the internal flow in the melt is stable buoyant−thermocapillary convection. With the Marangoni number increasing, the flow intensity of toroidal roll cells is strengthened; while the Marangoni number exceeds a certain critical value, the stable flow transits to unsteady buoyant−thermocapillary convection.

2) With the dimensionless height of melt increasing, the flow in the melt is enhanced at first and then weakens, but the change is slight. As the width of gap decreases gradually, the strength of flow is enhanced. At the same time, the critical Marangoni number increases slightly with a greater melt height, and increases with a narrower width of gap.

3) The present of axial magnetic field plays an important role in suppressing the buoyant−thermocapillary convection in the melt, and the suppression is more evident as magnetic field gets stronger. The critical Marangoni number depends on the intensity of axial magnetic field. The stronger the intensity of axial magnetic field, the larger the critical Marangoni number.

References

[1] YUE J T, VOLTMER F W. Influence of gravity-free solidification on solute micro-segregation [J]. Journal of Crystal Growth, 1975, 29(3): 329−341.

[2] WITT A F, GATOS H C, LICHTENSTEIGER M , LAVINE M C, HERMAN C J. Crystal growth and steady-state segregation under zero gravity: InSb [J]. Journal of the Electrochemical Society, 1975, 122(2): 276−283.

[3] SYLLA L, DUFFAR T. Experimental investigation of dewetting models [J]. Journal of Crystal Growth, 2011, 324(1): 53−62.

[4] GAMAL G A, ABOU ZIED M, EBNALWALED A A. Mobility improvement by detached solidification of CZT crystals [J]. Physica B: Condensed Matter, 2007, 396(1): 155−159.

[5] PENG Lan, FAN Ju-yan, LI You-rong. Numerical simulation of thermocapillary convection in detached solidification under microgravity [J]. Microgravity Science and Technology, 2008, 20(3−4): 231−235.

[6] PENG Lan, FAN Ju-yan, LI You-rong, MENG Hai-yong. Two-dimensional numerical simulation of thermocapillary convection in detached solidification [J]. Science China: Technological Sciences, 2012, 55(2): 527−536.

[7] ZHANG H, LARSON D J, WANG C L, CHEN T H. Kinetics and heat transfer of CdZnTe Bridgman growth without wall contact [J]. Journal of Crystal Growth, 2003, 250(1): 215−222.

[8] STELIAN C, YECKEL A, DERBY J J. Influence of thermal phenomena on crystal reattachment during dewetted Bridgman growth [J]. Journal of Crystal Growth, 2009, 311(8): 2572−2579.

[9] WU Meng-hua, LIU Xin-gong, WANG Yuan-gang, JIA Wei-ping. Simulation of electrodeposition process based on electromagnetic coupling with flow field [J]. The Chinese Journal of Nonferrous Metals, 2013, 23(1): 219−228. (in Chinese)

[10] LI Ming-wei, HU Wen-rui, CHEN Nuo-fu, ZENG Dan-ling, TANG Ze-mei. Numerical analysis of LEC growth of GaAs with an axial magnetic field [J]. International Journal of Heat and Mass Transfer, 2002, 45(13): 2843−2851.

[11] CHENG Cong-qian, HUANG Ming-liang, ZHAO Jie, XUE Dong-feng. Effect of uniform magnetic field on crystallization of intermetallic compound layers between Cu and liquid SnZn alloys [J]. Transactions of Nonferrous Metals Society of China, 2012, 22: 2312−2319.

[12] HU Xiao-wu, LI Shuang-ming, GAO Si-feng, LIU Lin, FU Heng-zhi. Effect of melt convection on primary dendrite arm spacing in directionally solidification Pb−26%Bi hypo-peritectic alloys [J]. Transactions of Nonferrous Metals Society of China, 2011, 21: 65−71.

[13] GELFGAT A Y, BAR-YOSEPH P Z, SOLAN A. Effect of axial magnetic field on three-dimensional instability of natural convection in a vertical Bridgman growth configuration [J]. Journal of Crystal Growth, 2001, 230(1): 63−72.

[14] JABER T J, SAGHIR M Z, VIVIANI A. Three-dimensional modelling of GeSi growth in presence of axial and rotating magnetic fields [J]. European Journal of Mechanics B: Fluids, 2009, 28(2): 214−223.

[15] SANKAR M, VENKATACHALAPPA M, DO Y. Effect of magnetic field on the buoyancy and thermocapillary driven convection of an electrically conducting fluid in an annular enclosure [J]. International Journal of Heat and Fluid Flow, 2011, 32(2): 402−412.

[16] PENG Lan, MENG Hai-yong, LI Zhen. Axial magnetic field influence on thermocapillary convection in detached solidification under microgravity [J]. Microgravity Science and Technology, 2011, 23: 141−147.

[17] PENG Lan, ZHOU Ling-min, LI You-rong, WEN Jin-xiong. Effect of cusp magnetic field on CdZnTe crystal growth by detached solidification [J]. Journal of Engineering Thermophysics, 2012, 33(4): 565−568. (in Chinese)

[18] LI Y R, IMAISHI N, AZAMI T, HIBIYA T. Three-dimensional oscillatory flow in a thin annular pool of silicon melt [J]. Journal of Crystal Growth, 2004, 260(1): 28−42.

几何因素和轴向磁场对分离结晶过程中熔体浮力−热毛细对流的影响

李 震，彭 岚，李友荣

重庆大学 低品位能源利用技术及系统教育部重点实验室，重庆 400044

摘 要：为了研究几何因素和轴向磁场对分离结晶过程中熔体浮力−热毛细对流的影响，采用有限差分法进行三维数值模拟。结果表明，当 Marangoni 数较小时，熔体内部流动为稳态浮力−热毛细对流；随着 Marangoni 数的增大并超过一定值，稳态流动转变为非稳态浮力−热毛细对流。随着熔体高度的增加，熔体内部流动先增强后减弱；随着狭缝宽度的减小，熔体流动增强。采用轴向磁场能够有效抑制熔体内浮力热−毛细对流，随着磁场强度的增加，抑制效果逐渐增强。流动失稳的临界 Marangoni 数随着熔体高度的增加而略有增大，随着狭缝宽度的减小而增大，随着磁场强度的增大而增大。

关键词：晶体生长；分离结晶；浮力−热毛细对流；轴向磁场

(Edited by Hua YANG)